Coil excited Pseudo Direct Drive electrical machines

A. Penzkofer, G. Cooke, M. Odavic, and K. Atallah

Department of Electronic and Electrical Engineering, University of Sheffield, Sheffield S1 3JD, U.K.

A Pseudo Direct Drive (PDD) equipped with a coil excited high-speed (HS) rotor is presented. An analytical model which predicts the flux density in the air spaces and permanent magnets (PM) of the PDD is presented, and it is shown, that a good agreement exists between the analytical and finite element (FE) predictions. Furthermore, the model is employed to investigate the effects of the key design parameters on the performance of a coil excited PDD for a 10MW wind turbine application and an optimised design is proposed. It is shown that shear stress in excess of 100kPa can be achieved, and that compared to a PM excited PDD a reduction in PM mass can be realized. It is also shown that the efficiency over the operating range of the wind turbine can be maximized by adopting an appropriate control strategy of the HS rotor excitation currents.

Index Terms—Pseudo Direct Drive, magnetic gear, wind turbine

I. Introduction

Magnetic gears (MG) can be an alternative solution to mechanical gears in many applications and have increasingly received attention by industry and research in the recent decades [1]. Because of the contactless torque transmission capability and the inherent overload protection, reliability can be significantly improved. A particular promising design with torque densities similar to those of mechanical gearboxes is the concentric MG [2],[3]. Furthermore, stator windings may be added to form a magnetically geared machine [1],[4],[5]. A design which only requires two mechanical airgaps and where the PMs with the higher pole-number is fixed to the stator is presented by the Pseudo Direct Drive (PDD) [5]. Due to the compact integration of the magnetic gearing element within the machine these types of machines could enable the realisation of light-weight and compact drive-train solutions for many applications, such as wind turbines [6]. However, despite their many advantages a concern for the application of wind remains the relatively larger quantities of permanent magnets (PM) required for their realisation [7]. Therefore, while PDDs have so far been designed and manufactured with PM excitation on both the high-speed (HS) rotor and the stator, it is proposed that in order to reduce the PM mass and introduce an extra degree of controllability, that the HS rotor is excited using coils supplied with a dc current. Fig. 1 shows a schematic of a coil excited PDD where the PMs on the HS rotor are replaced with a winding supplied with a dc current.

The novel design for a coil excited PDD has been considered for a 10MW wind turbine. In order to achieve an efficient and economically feasible design optimisation studies have been conducted in this work. Generally is the optimisation of the PDD essential to achieve a light-weight and cost effective drive train solution. However, the optimisation may involve investigating into the effects of many variables and hence large amounts of data. Although

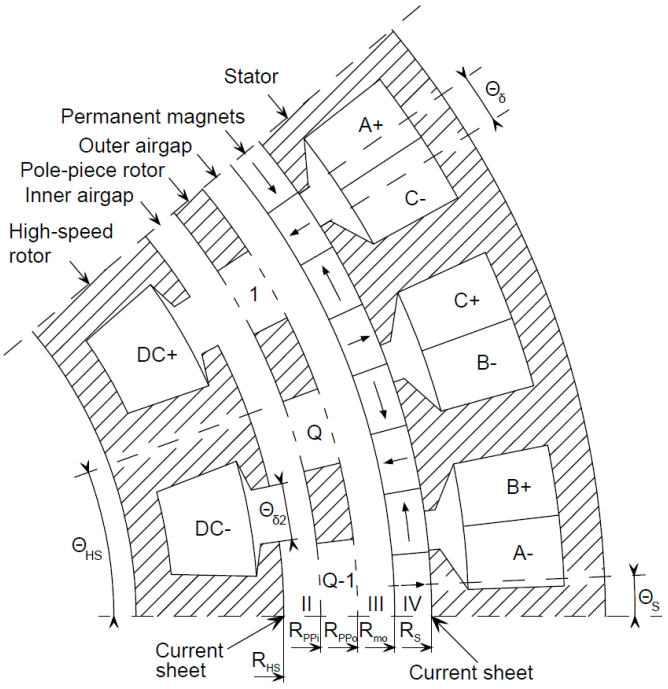

Fig. 1. Schematic of a PDD segment. The PMs on the stator are magnetised in discrete Halbach arrangement.

finite element (FE) analysis may enable an accurate analysis of the PDD it also could require in a significant computational effort. An analytical model has been proposed in [7]-[9] for the prediction of the flux density distribution in the PM and air regions of PDDs with HS rotor PM excitation. In this paper an analytical model for the prediction of the flux density distributions in the air spaces and PMs of a PDD with coil excited HS rotor is presented. It employs similar methodology to the one adopted for the PM excited HS rotor PDD, and the HS rotor coils and the stator coils are represented by equivalent current sheets. The model is employed to investigate the effects of the key design parameters on the key performance indicators of the PDD, such as mass and efficiency. However, a design has been selected for a more detailed analysis using FE method. It is shown, that replacing the PMs on the HS rotor of a PDD with windings can result in

Color versions of one or more of the figures in this paper are available online at http://ieeexplore.ieee.org.

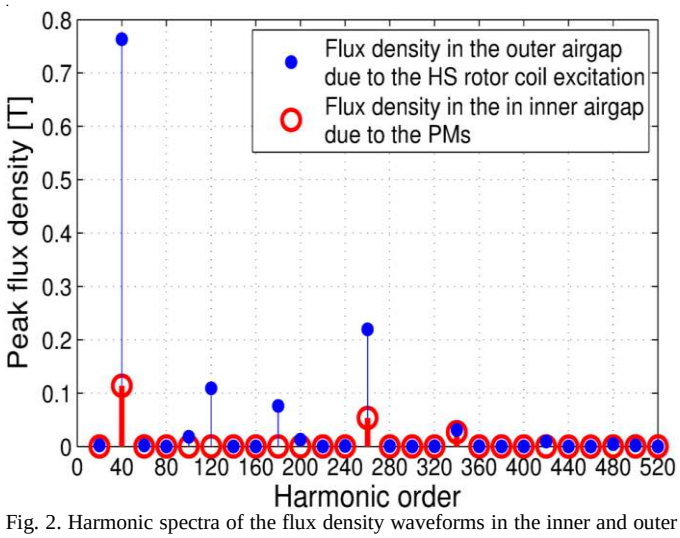

Fig. 2. Harmonic spectra of the flux density waveforms in the inner and outer airgap due to the HS rotor coil excitation and the PMs respectively.

reductions in PM mass, and that shear stress in excess of 100kPa can be achieved. It is also shown that the control strategy, more specifically the variation of the dc excitation current with wind speed, has a significant effect on the efficiency of the coil excited PDD. Therefore, in summary a coil excited PDD is proposed together with an analytical model for the prediction of its key design parameters. The analysis and design optimisation is focused on a 10MW wind turbine.

II. Principle of Operation

Similarly to the PM excited PDD the windings on the HS rotor interact with the windings on the stator to produce electromagnetic torque, which is transferred to the pole-piece (PP) rotor by the interaction of the windings on the HS rotor and the PMs on the stator. Fig. 2 shows the harmonic spectra of the flux density waveforms in the airgaps adjacent to the stator and the HS rotor, due to the windings on the HS rotor and the PMs on the stator, respectively. It can be seen that the introduction of the ferromagnetic PPs results in a dominant 260 pole-pair asynchronous space harmonic field which interacts with the stationary PMs to transmit torque, while the 40 pole-pair synchronous harmonic interacts with the stator winding to produce electromagnetic torque in a similar manner to a wound rotor synchronous machine.

The equations which govern the motion of the turbine, the HS rotor and the PP rotor are

$$J_T \frac{d^2\theta_T}{dt^2} = T_W - k_S(\theta_T - \theta_{PP}) \tag{1}$$

$$J_{PP} \frac{d^2\theta_{PP}}{dt^2} = k_S(\theta_T - \theta_{PP}) - T_{pull}(I_f)\sin(Q\theta_{PP} - p_{HS}\theta_{HS}) \tag{2}$$

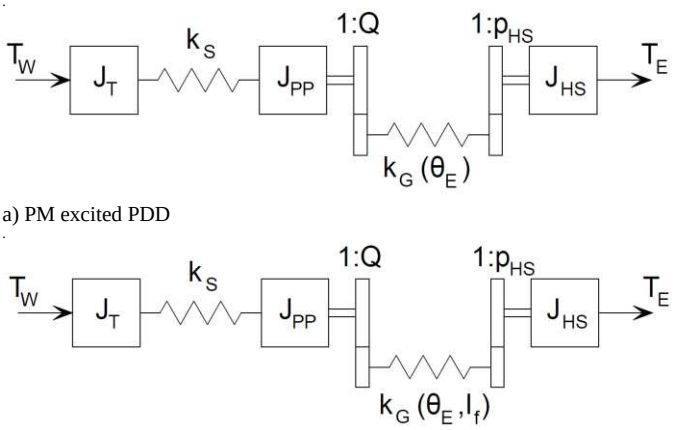

Fig. 3. 3-inertia torsional model of a wind turbine employing a PDD.

$$J_{HS} \frac{d^2\theta_{HS}}{dt^2} = \frac{p_{HS}}{Q} T_{pull}(I_f)\sin(Q\theta_{PP} - p_{HS}\theta_{HS}) - T_E(I_f, I_S) \tag{3}$$

where J_T is the inertia of the turbine, J_{HS} is the inertia of the HS rotor, and J_{PP} is the inertia of the PP rotor and the inertias of the components connected to it, such as the shaft and the turbine. θ_T, θ_{HS} and θ_{PP} are the angular positions of the turbine, the HS rotor, and the PP rotor respectively, and p_{HS} and Q are the number of pole-pairs on the HS rotor and the number of ferromagnetic PPs on the PP rotor. I_f is the magnitude of the dc current in the HS rotor windings, and I_S is the magnitude of the rms current in the stator windings. T_{pull}, T_W, and T_E are the pullout torque of the MG element of the PDD, the torque supplied by the wind, and the electromagnetic torque, respectively. k_S is the stiffness of the shaft connecting the turbine to the PP rotor.

Fig. 3 shows the torsional models of a wind turbine drive train employing PM excited and coil excited PDDs. It can be seen that the MG element of the PDD can be replaced by two ideal gears and a 1-to-1 magnetic coupling, having a stiffness k_G given by

$$k_G = \frac{T_{pull}(I_f)}{Q}\cos(Q\theta_{PP} - p_{HS}\theta_{HS}) = \frac{T_{pull}(I_f)}{Q}\cos(\theta_E) \tag{4}$$

where θ_E is the referred load angle. In a PM excited PDD k_G is only a function of θ_E, while in a coil excited PDD k_G is also a function of I_f. This should be taken into consideration, when controlling such a PDD. From equations (1)-(3) it can be seen, that the MG element of the PDD is essentially a compliant transmission which could isolate the mechanical drive line from shock loads caused by the electrical system, such as transient and short circuit currents. And hence improving the reliability of the mechanical drive line and reducing its size since it would not be subjected to the electrically produced overload torques. However, the inherent compliance of the magnetic transmission should be carefully considered in the design and control of the drive train, since it would introduce low frequency oscillatory modes.

III. Analytical model

The methodology which has been employed to develop the analytical technique for the prediction of the flux density distributions in the airgaps and PM regions of MGs and PDDs with PM excitation on HS rotor and stator [7],[8],[9], is adopted for the development of the analytical model for the prediction of the flux density distribution in the airgap and PM regions of the coil excited PDD. The effects of the stator and the HS rotor windings are accounted for by currents sheets on the stator iron bore diameter and the HS rotor outer diameter, respectively. End effects are neglected and the iron is assumed to be infinitely permeable.

The Maxwell equations for quasi-static conditions are

$$\nabla \vec{B} = 0 \tag{5}$$

$$\nabla \times \vec{H} = \vec{J} \tag{6}$$

where $\vec{H}$ is the magnetic field strength, $\vec{J}$ is the current density, and $\vec{B}$ is the magnetic flux density. $\vec{B}$ is related to $\vec{H}$ by

$$\vec{B} = \mu_0 \vec{H} \quad \text{in air regions} \tag{7}$$

$$\vec{B} = \mu_0 \mu_r \vec{H} + \mu_0 \vec{M} \quad \text{in PM regions} \tag{8}$$

where μ_0 is the permeability in air, μ_r is the relative permeability of the PMs, and $\vec{M}$ is the residual magnetisation. Furthermore the flux density is given by $\vec{B} = \nabla \times \vec{A}$, where $\vec{A}$ is the vector potential. $\vec{A}$ is given by solving the Laplace and Poisson equations

$$\Delta \vec{A} = 0 \quad \text{in the air regions} \tag{9}$$

$$\Delta \vec{A} = -\mu_0 \nabla \times \vec{M} \quad \text{in the PM regions} \tag{10}$$

and applying the boundary conditions. Due to the symmetry in z, only the z-component A of the vector potential is non-zero. If A is expressed as a Fourier series, the coefficients of the Fourier series for the various regions are related by the boundary conditions at the interfaces. At the interfaces between the iron regions and the air/PM regions the tangential component of $\vec{H}$ is zero. Apart from the HS rotor outer radius R_{HS} and the stator bore radius R_S, where the tangential component of $\vec{H}$ is equal to the current sheet representing the HS rotor windings and the stator windings, respectively [10].

The circumferential component of $\vec{H}$ equals the current sheet at R_{HS}, hence

$$H_{\theta,II}(R_{HS},\theta) = \frac{1}{\mu_0} B_{\theta,II}(R_{HS},\theta) = -J_{HS}(\theta) \tag{11}$$

where $H_{\theta,II}$ and $B_{\theta,II}$ are the circumferential components of the magnetic field and flux density in region II, respectively. J_{HS} is the current sheet representing the effects of the HS rotor windings and it is expressed as a Fourier series by the coefficients $J_{HS,A,n}$ and $J_{HS,C,n}$ as

$$J_{HS}(\theta) = \sum_{n=1}^{\infty} \begin{pmatrix} J_{HS,A,n} \\ J_{HS,C,n} \end{pmatrix} \cdot \begin{pmatrix} cos(n\theta) \\ sin(n\theta) \end{pmatrix} \tag{12}$$

Similarly, at R_S the circumferential component of $\vec{H}$ equals the current sheet, hence

$$H_{\theta,IV}(R_S,\theta) = \frac{B_{\theta,IV}(R_S,\theta)}{\mu_0 \mu_r} - \frac{M_{\theta,IV}(\theta)}{\mu_r} = -J_s(\theta) \tag{13}$$

where $H_{\theta,IV}$, $B_{\theta,IV}$ and $M_{\theta,IV}$ are the circumferential components of $\vec{H}$, $\vec{B}$ and $\vec{M}$ in region IV, respectively. J_S is the current sheet at the stator bore radius representing the effects of the stator windings and it is expressed as a Fourier series by the coefficients $J_{S,A,n}$ and $J_{S,C,n}$ as

$$J_S(\theta) = \sum_{n=1}^{\infty} \begin{pmatrix} J_{S,A,n} \\ J_{S,C,n} \end{pmatrix} \cdot \begin{pmatrix} cos(n\theta) \\ sin(n\theta) \end{pmatrix} \tag{14}$$

The vector potentials for the air gap regions II and III, and the PP air regions 1,..,Q given in [8] can be expressed as

$$A_{II}(r,\theta) = A_{II,0} + \sum_{n=1}^{\infty} \left\{ \frac{R_{HS}}{n} \frac{P_n(r,R_{PPi})}{E_n(R_{HS},R_{PPi})} \begin{pmatrix} A_{II,n} \\ C_{II,n} \end{pmatrix} + \frac{R_{PPi}}{n} \frac{P_n(r,R_{HS})}{E_n(R_{PPi},R_{HS})} \begin{pmatrix} B_{II,n} \\ D_{II,n} \end{pmatrix} \right\} \cdot \begin{pmatrix} \cos n\theta \\ \sin n\theta \end{pmatrix} \tag{15}$$

$$A_{III}(r,\theta) = A_{III,0} + \sum_{n=1}^{\infty} \left\{ \frac{R_{PPo}}{n} \frac{P_n(r,R_{mo})}{E_n(R_{PPo},R_{mo})} \begin{pmatrix} A_{III,n} \\ C_{III,n} \end{pmatrix} + \frac{R_{mo}}{n} \frac{P_n(r,R_{PPo})}{E_n(R_{mo},R_{PPo})} \begin{pmatrix} B_{III,n} \\ D_{III,n} \end{pmatrix} \right\} \cdot \begin{pmatrix} \cos n\theta \\ \sin n\theta \end{pmatrix} \tag{16}$$

$$A_i(r,\theta) = R_{PPi} \left(A_{i,0} + B_{i,0} \ln \frac{r}{R_{PPi}} \right) + \sum_{n=1}^{\infty} R_{PPi} \left\{ \frac{E_{n\pi/\beta}(r,R_{PPo})}{E_{n\pi/\beta}(R_{PPi},R_{PPo})} A_{i,n} + \frac{E_{n\pi/\beta}(r,R_{PPi})}{E_{n\pi/\beta}(R_{PPi},R_{PPo})} B_{i,n} \right\} \cos(n\pi(\theta - \theta_i)/\beta) \tag{17}$$

where R_{PPi}, R_{PPo} and R_{mo} are radii shown in Fig. 1, β is the PP opening angle, θ_i is the angular position of the i-th slot, and

$$P_n(v,w) = \left(\frac{v}{w}\right)^n + \left(\frac{v}{w}\right)^{-n} \tag{18}$$

$$E_n(v,w) = \left(\frac{v}{w}\right)^n - \left(\frac{v}{w}\right)^{-n} \tag{19}$$

are functions of values v and w. The solution for the vector potential in the PM region IV is given by [9]:

$$A_{IV}(r,\theta) = A_{G,IV}(r,\theta) + A_{P,IV}(r,\theta) + A_{C,IV}(r,\theta) \tag{20}$$

where $A_{G,IV}$ is the general solution and $A_{P,IV}$ is a particular solution of equation (10) without a current sheet, and $A_{C,IV}$ is accounting for the effects of the current sheet. For a discrete Halbach magnetisation these take the form:

$$A_{G,IV}(r,\theta) = \sum_{n=1}^{\infty} \frac{P_n(r,R_S)}{P_n(R_{mo},R_S)} \begin{pmatrix} A_{IV,n} \\ C_{IV,n} \end{pmatrix} \cdot \begin{pmatrix} cos(n\theta) \\ sin(n\theta) \end{pmatrix} \quad (21)$$

$$A_{P,IV}(r,\theta) = B_r \sum_{n=1}^{\infty} X_n(r) \begin{pmatrix} sin(n\Theta_S) \\ -cos(n\Theta_S) \end{pmatrix} \cdot \begin{pmatrix} cos(n\theta) \\ sin(n\theta) \end{pmatrix} \quad (22)$$

$$A_{C,IV}(r,\theta) = \mu_0\mu_r \sum_{n=1}^{\infty} \frac{R_S}{n} \begin{pmatrix} J_{S,A,n} \\ J_{S,C,n} \end{pmatrix} \cdot \begin{pmatrix} cos(n\theta) \\ sin(n\theta) \end{pmatrix} \times \left\{ \left(\frac{r}{R_S}\right)^n - \frac{P_n(r,R_S)}{P_n(R_{mo},R_S)} \left(\frac{R_{mo}}{R_S}\right)^n \right\} \quad (23)$$

where B_r is the remanence of the PMs, and Θ_S is an angle dependent on the stator PMs positions, shown in Fig. 1. The function $X_n(r)$ depends on the magnetisation and it is given by

$$X_n(r) = h_{n,m_S,p_S} \left(Y_n(r) - \frac{P_n(r,R_S)}{P_n(R_{mo},R_S)} Y_n(R_{mo}) \right) \quad (24)$$

$$h_{n,m_S,p_S} = \frac{m_S p_S}{\pi} \frac{sin\left(n\frac{\pi}{m_S p_S}\right)}{n} \epsilon_{n,p_S} \quad (25)$$

$$Y_n(r) = \frac{R_S}{n} \left(\frac{r}{R_S}\right)^n G_n + f_n(r)(n\epsilon^+_{n,m_S,p_S} + \epsilon^-_{n,m_S,p_S}) \quad (26)$$

$$f_n(r) = \begin{cases} r\dfrac{1}{1-n^2} & n > 1 \\ \dfrac{1}{2} r\, ln(r) & n = 1 \end{cases} \quad (27)$$

$$\epsilon^+_{n,m,p_S} = \epsilon_{m_S p_S, n-p_S} + \epsilon_{m_S p_S, n+p_S} \quad (28)$$

$$\epsilon^-_{n,m,p_S} = \epsilon_{m_S p_S, n-p_S} - \epsilon_{m_S p_S, n+p_S} \quad (29)$$

$$G_n = -\left(n\epsilon^+_{n,m_S,p_S} + \epsilon^-_{n,m_S,p_S}\right) \frac{\partial f_n}{\partial r}(R_S) + \epsilon^-_{n,m_S,p_S} \quad (30)$$

$$\epsilon_{n,p_S} = \begin{cases} 1 & n \ mod \ p_s = 0 \\ 0 & n \ mod \ p_s \neq 0 \end{cases} \quad (31)$$

where p_S is the number of pole-pairs on the stator, m_S is the number of Halbach segments per pole-pair, and $n \ mod \ p_s$ is the modulo operation.

Applying the boundary condition (11) gives the following relation for the coefficients of region II and the current sheet:

$$\begin{pmatrix} A_{II,n} \\ C_{II,n} \end{pmatrix} = \mu_0 \begin{pmatrix} J_{HS,A,n} \\ J_{HS,C,n} \end{pmatrix} \quad (32)$$

The boundary conditions at the interface between region III and IV:

$$B_{rad,III}(R_{mo},\theta) = B_{rad,IV}(R_{mo},\theta) \quad (33)$$

$$B_{\theta,III}(R_{mo},\theta) = \frac{1}{\mu_r}(B_{\theta,IV}(R_{mo},\theta) - \mu_0 M_{\theta,IV}(\theta)) \quad (34)$$

give the following relations between coefficients of regions III and IV [9]:

$$\begin{pmatrix} A_{IV,n} \\ C_{IV,n} \end{pmatrix} = \begin{pmatrix} B_{III,n} \\ D_{III,n} \end{pmatrix} \frac{P_n(R_{mo},R_{PPo})}{E_n(R_{mo},R_{PPo})} + \begin{pmatrix} A_{III,n} \\ C_{III,n} \end{pmatrix} \frac{2}{E_n(R_{PPo},R_{mo})} \quad (35)$$

$$\begin{pmatrix} B_{III,n} \\ D_{III,n} \end{pmatrix} = \frac{1}{\mu_r} \begin{pmatrix} A_{IV,n} \\ C_{IV,n} \end{pmatrix} \frac{E_n(R_{mo},R_S)}{P_n(R_{mo},R_S)} + \mu_0 \left(\frac{R_{mo}}{R_S}\right)^{n-1} \left\{ 1 - \frac{E_n(R_{mo},R_S)}{P_n(R_{mo},R_S)} \right\} \begin{pmatrix} J_{s,A,n} \\ J_{s,C,n} \end{pmatrix} + \frac{B_r}{\mu_r} \left(-h_{n,m_S,p_S} \epsilon^-_{n,m_S,p_S} + X'_n(R_{mo}) \right) \begin{pmatrix} \sin(n\Theta_S) \\ -\cos(n\Theta_S) \end{pmatrix} \quad (36)$$

where $X'_n(r)$ is the derivative of $X_n(r)$. The boundary conditions at the interfaces between the air gap region II and III, and the PP air regions lead to the following set of relations between coefficients of regions II, III and $1,\ldots,Q$ [8]:

$$\begin{pmatrix} B_{II,n} \\ D_{II,n} \end{pmatrix} = \sum_{i=1}^{Q} \left\{ \frac{B_{i,0}}{\pi} \begin{pmatrix} r(n,i) \\ s(n,i) \end{pmatrix} + \sum_{k=1}^{\infty} \frac{k}{\beta} \left[\frac{P_{k\pi/\beta}(R_{PPi},R_{PPo})}{E_{k\pi/\beta}(R_{PPi},R_{PPo})} A_{i,k} - \frac{2}{E_{k\pi/\beta}(R_{PPi},R_{PPo})} B_{i,k} \right] \begin{pmatrix} f(k,n,i) \\ g(k,n,i) \end{pmatrix} \right\} \quad (37)$$

$$\begin{pmatrix} A_{III,n} \\ C_{III,n} \end{pmatrix} = \sum_{i=1}^{Q} \frac{R_{PPi}}{R_{PPo}} \left\{ \frac{B_{i,0}}{\pi} \begin{pmatrix} r(n,i) \\ s(n,i) \end{pmatrix} + \sum_{k=1}^{\infty} \frac{k}{\beta} \left[\frac{2}{E_{k\pi/\beta}(R_{PPi},R_{PPo})} A_{i,k} - \frac{P_{k\pi/\beta}(R_{PPi},R_{PPo})}{E_{k\pi/\beta}(R_{PPi},R_{PPo})} B_{i,k} \right] \begin{pmatrix} f(k,n,i) \\ g(k,n,i) \end{pmatrix} \right\} \quad (38)$$

$$A_{i,k} = \sum_{n=1}^{\infty} \frac{2}{n\beta} \left\{ \frac{R_{HS}}{R_{PPi}} \frac{2}{E_n(R_{HS},R_{PPi})} \begin{pmatrix} A_{II,n} \\ C_{II,n} \end{pmatrix} - \frac{P_n(R_{HS},R_{PPi})}{E_n(R_{HS},R_{PPi})} \begin{pmatrix} B_{II,n} \\ D_{II,n} \end{pmatrix} \right\} \cdot \begin{pmatrix} f(k,n,i) \\ g(k,n,i) \end{pmatrix} \quad (39)$$

$$B_{i,k} = \sum_{n=1}^{\infty} \frac{2}{n\beta} \left\{ \frac{R_{PPo}}{R_{PPi}} \frac{P_n(R_{PPo},R_{mo})}{E_n(R_{PPo},R_{mo})} \begin{pmatrix} A_{III,n} \\ C_{III,n} \end{pmatrix} - \frac{R_{mo}}{R_{PPi}} \frac{2}{E_n(R_{PPo},R_{mo})} \begin{pmatrix} B_{III,n} \\ D_{III,n} \end{pmatrix} \right\} \cdot \begin{pmatrix} f(k,n,i) \\ g(k,n,i) \end{pmatrix} \quad (40)$$

$$A_{i,0} = A_{II,0} + \sum_{n=1}^{\infty} \frac{2}{n\beta} \left\{ \frac{R_{HS}}{R_{PPi}} \frac{2}{E_n(R_{HS},R_{PPi})} \begin{pmatrix} A_{II,n} \\ C_{II,n} \end{pmatrix} - \frac{P_n(R_{HS},R_{PPi})}{E_n(R_{HS},R_{PPi})} \begin{pmatrix} B_{II,n} \\ D_{II,n} \end{pmatrix} \right\} \cdot \begin{pmatrix} r(n,i) \\ s(n,i) \end{pmatrix} \quad (41)$$

TABLE I
PARAMETERS OF A PDD FOR A 10MW WIND TURBINE

Quantity	Value
Pullout torque of the MG component [MNm]	11.9
Number of identical segments	20
Gear ratio	7.5
Pole-pieces per segment	15
Pole-pairs on HS rotor per segment	2
Pole-pairs on LS rotor per segment	13
Halbach segments per pole-pair	4
Airgap diameter [m]	8.0
Length of airgaps [mm]	8.0
Active axial length [m]	1.22
Remanence of PMs [T]	1.25
Relative recoil permeability of PMs	1.05
Rated PP rotor speed [rpm]	9.6
Rated electrical frequency [Hz]	48
PM mass [tons]	4.5
Copper mass [tons]	20
Active steel mass [tons]	59
Electromagnetic efficiency at rated power [%]	95

$$A_{i,0} + B_{i,0} \ln \frac{R_{PPo}}{R_{PPi}} = A_{III,0} \tag{42}$$
$$+ \sum_{n=1}^{\infty} \frac{2}{n\beta} \left\{ \frac{R_{PPo}}{R_{PPi}} \frac{P_n(R_{PPo}, R_{mo})}{E_n(R_{PPo}, R_{mo})} \begin{pmatrix} A_{III,n} \\ C_{III,n} \end{pmatrix} - \frac{R_{mo}}{R_{PPi}} \frac{2}{E_n(R_{PPo}, R_{mo})} \begin{pmatrix} B_{III,n} \\ D_{III,n} \end{pmatrix} \right\} \cdot \begin{pmatrix} r(n,i) \\ s(n,i) \end{pmatrix}$$

where $f(k,n,i)$, $g(k,n,i)$, $r(n,i)$ and $s(n,i)$ are functions given in [8].

Table I gives the parameters of a 10MW coil excited PDD for a wind turbine, where the PP rotor is directly connected to the turbine. The developed analytical model has been compared with 2-d FE for the PDD in Table I. The accuracy of the analytical solution is determined by the highest harmonic orders that are employed for the Fourier series in the airgaps and PM regions. The matrix that has to be inverted in order to gain the values of the unknown coefficients is of the size N_{total}^2, where $N_{total} = 8N + (2N_Q + 2)Q$, where N is the highest order harmonic considered in the air and PM regions, and N_Q is the highest order harmonic considered in the PP air regions. The computational effort would, therefore, depend significantly on the purpose of the analysis. For example if only the transmitted torques are required, which would be the case for optimisation purposes, N should not be much larger than the highest number of pole pairs per section, e.g. for the design in Table I N should be larger than 13. However, if for example torque ripples are required N should be increased in order to capture the effects of the higher harmonics [7].

Fig. 4a) and Fig. 5a) show the variations of the radial flux densities in the inner and outer airgaps, respectively, when the rated stator current is applied and the HS rotor currents are turned off. Fig. 4b) and Fig. 5b) show the variations of the radial flux densities in the inner and outer airgaps, respectively, when the HS rotor current is applied and the stator is open circuit. Fig. 4c) and Fig. 5c) show the variations of the radial flux densities in the inner and outer airgaps, respectively, at full load. It can be seen that a good agreement exists between the FE and analytical predictions. However minor differences can be observed due to the slot openings.

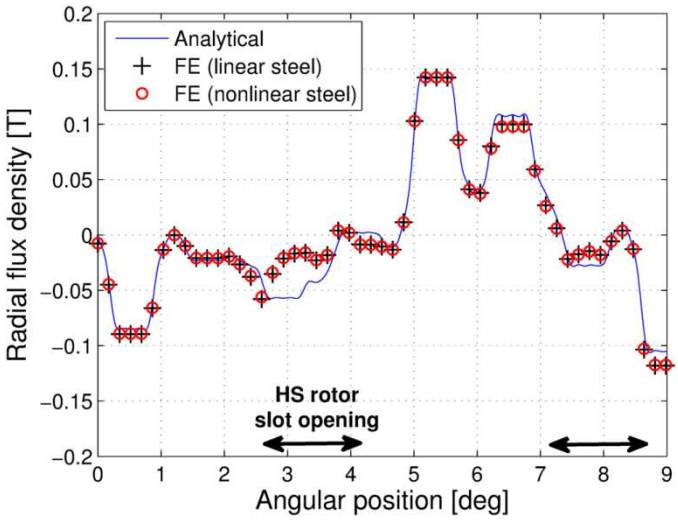

a) HS rotor currents are turned off.

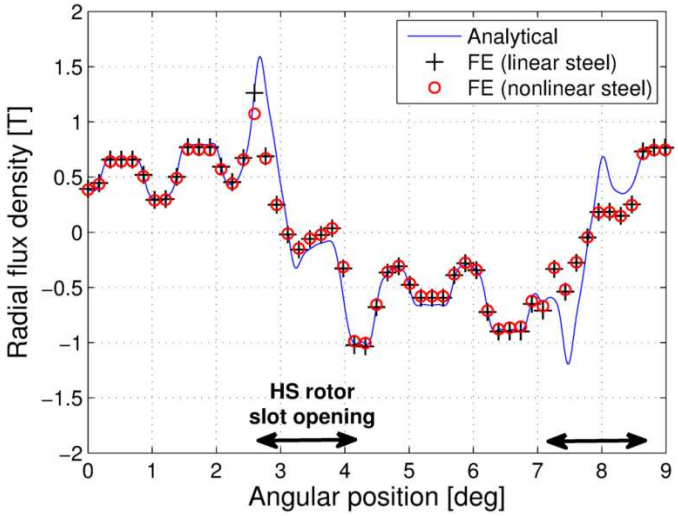

b) Stator currents are turned off.

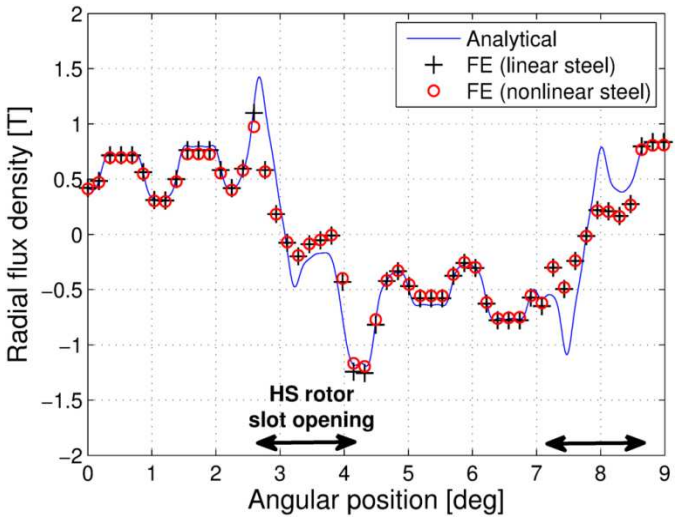

c) On load

Fig. 4. Variation of radial flux density with the angular position in the inner airgap.

Fig. 6 shows the electromagnetic torque on the PP rotor at pullout torque. It can be seen, that the torque calculated by FE is reduced, particularly for steel with non-linear characteristics, however the difference is only about 5%.

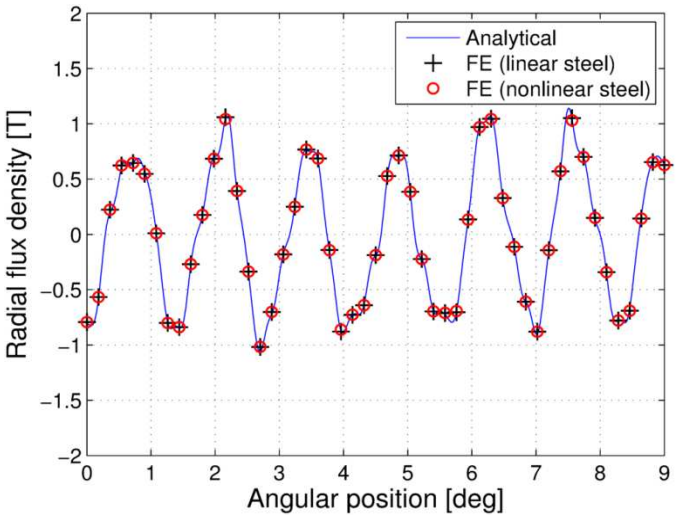

a) HS rotor currents are turned off.

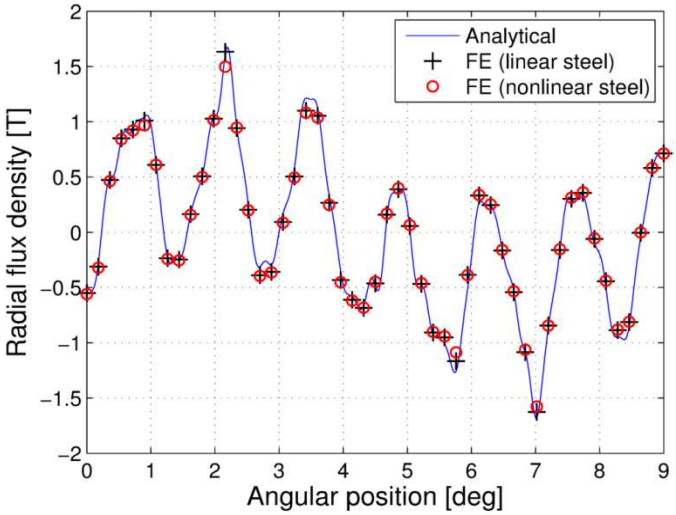

b) Stator currents are turned off.

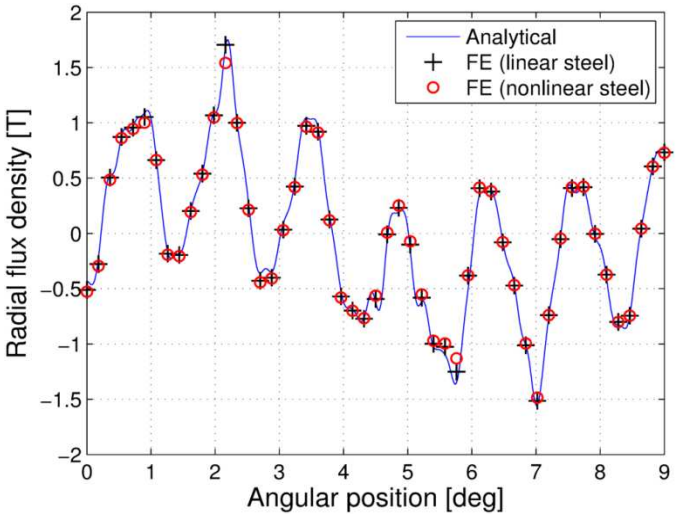

c) On load

Fig. 5. Variation of radial flux density with the angular position in the outer airgap.

Fig. 7 and Fig. 8 show the variations of the pullout torque and the fundamental component of the EMF with the current I_f, respectively. It can be seen, that the pullout torque and the EMF would initially vary linearly with I_f, however, saturation

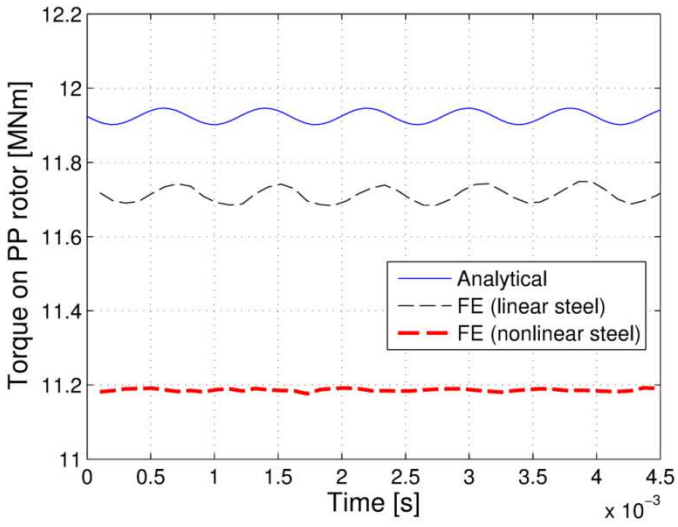

Fig. 6. Variation of the torque on the PP rotor at the pullout torque position with time.

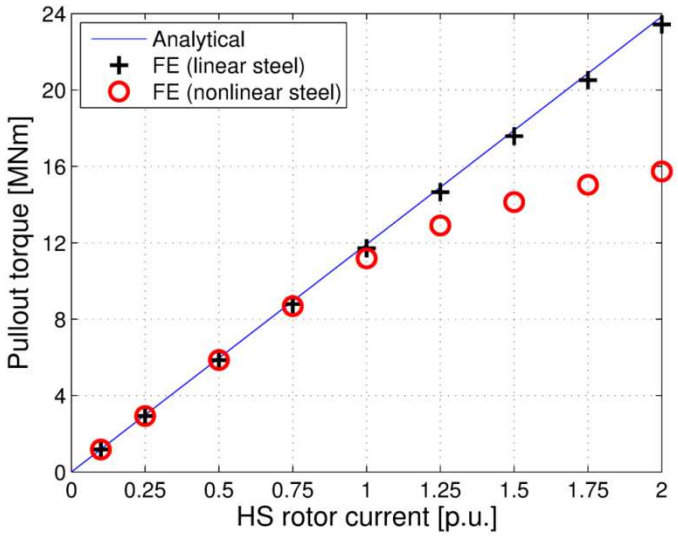

Fig. 7. Variation of the pullout torque with the HS rotor excitation current. (HS rotor current per unit of rated HS rotor current)

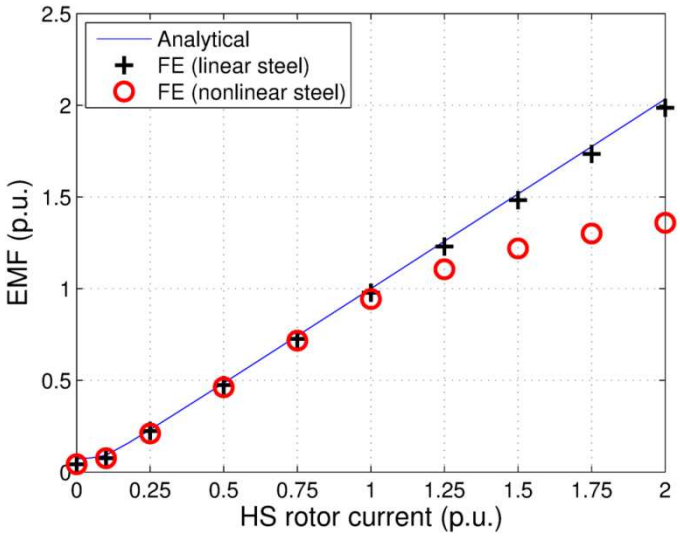

Fig. 8. Variation of the EMF with the HS rotor excitation current. (EMF per unit of the rated EMF and HS rotor current per unit of rated current)

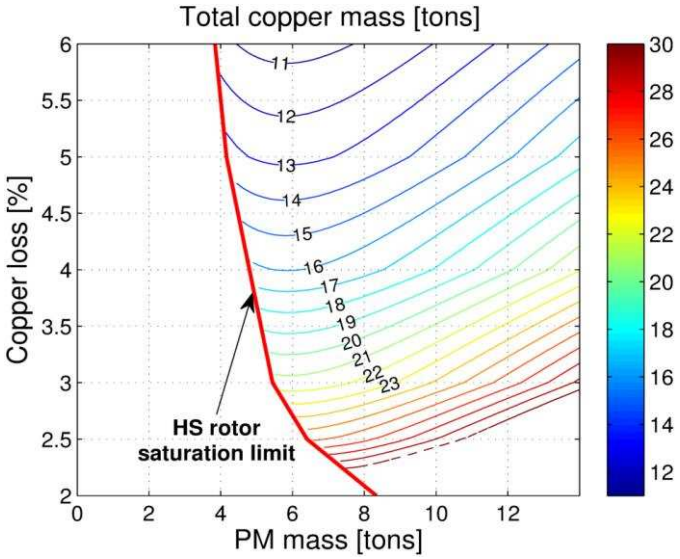

Fig. 9. Variation of copper mass with the PM mass and the total copper loss in percent of the rated power.

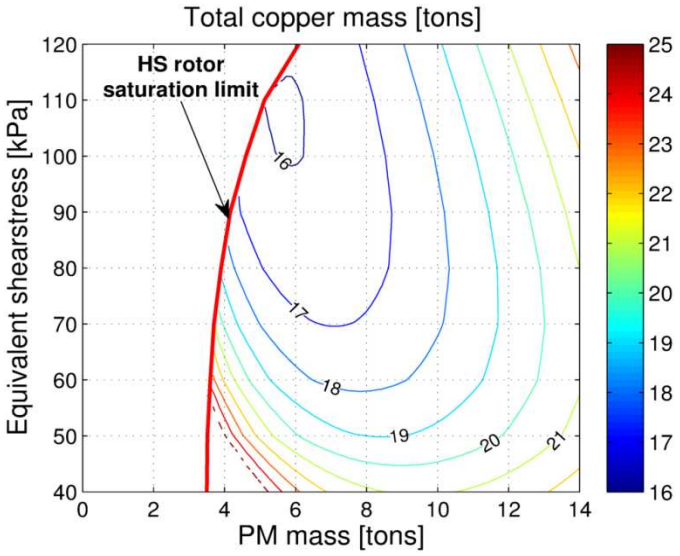

Fig. 11. Variation of copper mass with the PM mass and the equivalent shear stress at pullout torque, when the copper loss is fixed to 4.0%.

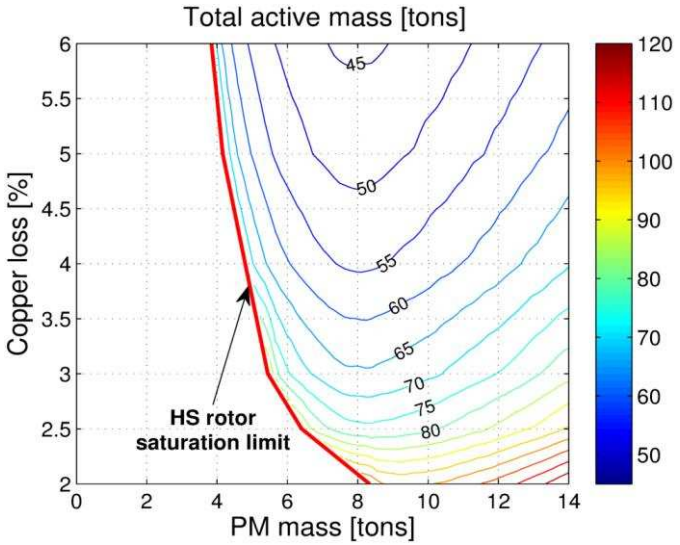

Fig. 10. Variation of total active mass with the PM mass and total copper loss in percent of the rated power.

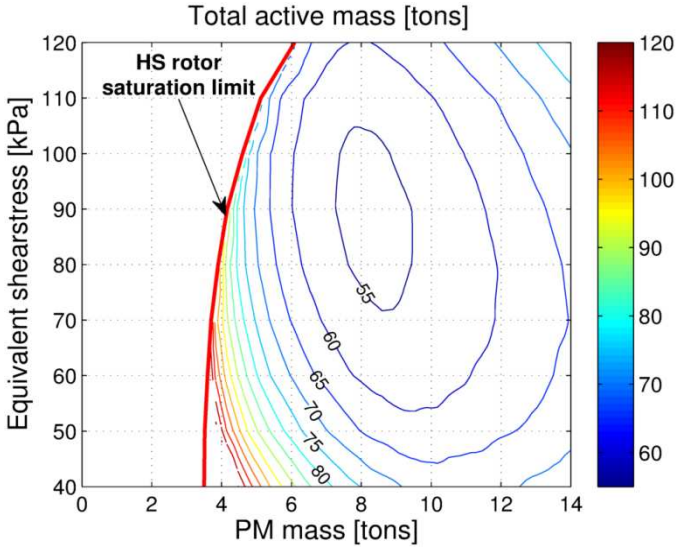

Fig. 12. Variation of total active mass with the PM mass and the equivalent shear stress at pullout torque, when the copper loss is fixed to 4.0%.

introduces a degree of non-linearity as I_f is increased, particularly beyond the rated value.

IV. Design of a 10MW PDD

The analytical techniques have been employed to study the effects of the main design parameters on the efficiency and masses of the active components of the PDDs for a 10MW wind turbine. For a PDD with the same airgap dimensions as the PDD given in Table I, Fig. 9 and Fig. 10 show the variations of the copper mass and the active mass, which includes the PM mass, the copper mass, and the laminated steel mass, with the PM mass and the loss in the copper windings, respectively. The iron loss has been neglected in this analysis, since for most of the considered designs it is the smaller loss component, with a contribution of about 1.0% of rated power. Only designs for which the flux density in the HS rotor iron teeth can be kept below 1.5T have been considered. For a given copper loss a minimum PM mass can be therefore achieved, which is due to saturation in the HS rotor teeth. It can be seen, that if the copper loss is decreased the minimum achievable PM mass and as expected the copper mass increases. It can also be seen, that for a given copper mass the copper loss may increase with increasing PM mass. Since an increase of PM mass would also increase the effective airgap length, this could lead to an increase of the required HS rotor current and therefore to increased copper losses. On the other hand, also the magnitude of the flux density due to the PMs would increase, which would decrease the required MMF produced by the HS rotor current. However, this would decrease the EMF, which would lead to an increase of the stator current and therefore also to increased copper losses. Finally it can be seen, that for a given copper mass a minimum copper loss can be achieved at about 6tons of PM material, while for a given total active mass a minimum copper loss can be achieved at about 8tons of PM material.

For the forthcoming analysis the copper loss is kept at 4.0%

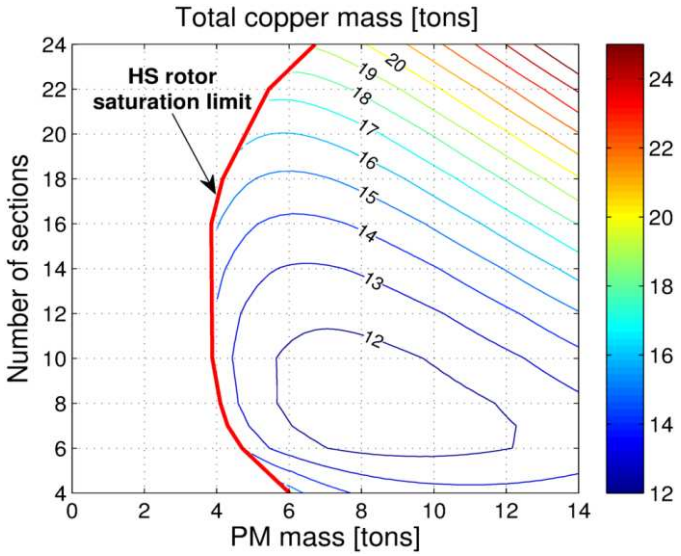

Fig. 13. Variation of copper mass with the PM mass and the number of segments, when the copper loss is fixed to 4.0%.

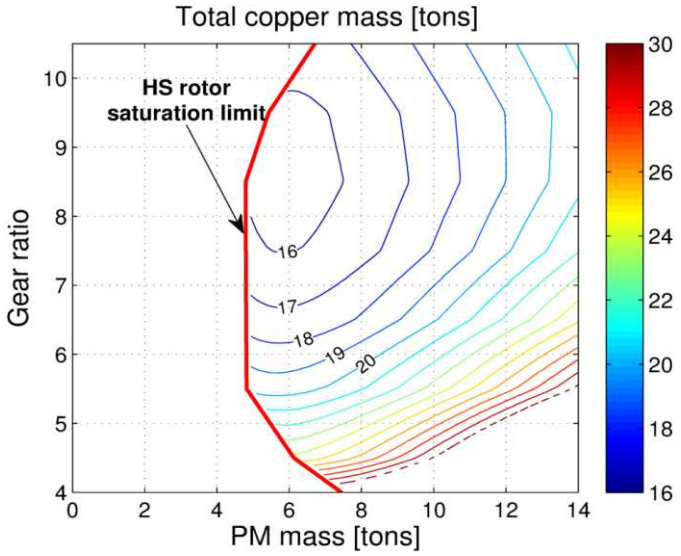

Fig. 15. Variation of copper mass with the PM mass and the gear ratio, when the copper loss is fixed to 4.0%.

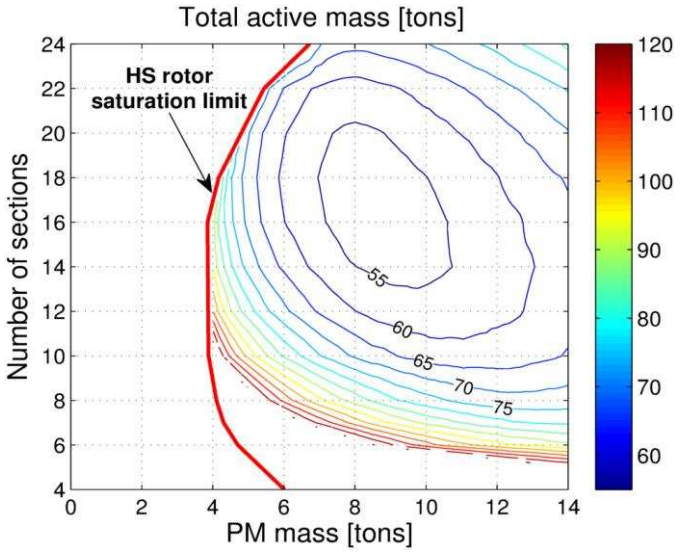

Fig. 14. Variation of total active mass with the PM mass and the number of segments, when the copper loss is fixed to 4.0%.

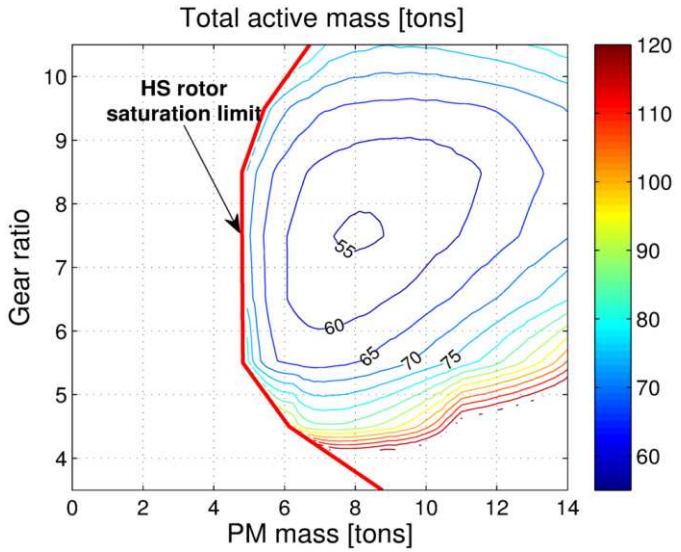

Fig. 16. Variation of total active mass with the PM mass and the gear ratio, when the copper loss is fixed to 4.0%.

of the rated power. For a gear ratio of 7.5 and the same airgap dimensions as the PDD in Table I, Fig. 11 and Fig. 12 show the variations of the copper mass and the active mass with the PM mass and the equivalent shearstress at pullout torque, where the equivalent shear stress at pullout torque is given by [9]:

$$\sigma_{pull} = \frac{2T_{pull}}{\pi D^2 l_a} \tag{43}$$

where D is the airgap diameter and l_a is the axial length. It can be seen, that designs with minimum copper mass or total active mass can be achieved, however the PM mass may not be minimum. Furthermore, a minimum PM mass of about 3.5tons can be achieved, however at the expense of increased copper and total active mass.

Due to the large size of the investigated PDDs, they are likely to be constructed from several circumferentially identical segments. Fig. 13 and Fig. 14 show the variations of the copper mass and the active mass, with the PM mass and the number of segments, where the equivalent shearstress at pullout torque is 100kPa. For each segment the numbers of pole-pairs and pole-pieces satisfy the following relationship in order to enable a gearing effect:

$$Q^* = p_{HS}^* + p_S^* \tag{44}$$

where Q^* is the number of pole-pieces per segment, p_{HS}^* is the number of pole-pairs on the HS rotor per segment, and p_S^* is the number of pole-pairs per segment on the stator. For the designs in Fig. 13 and Fig. 14 the same numbers of pole-pairs and pole-pieces per segment have been employed as for the PDD in Table I. Hence the gear ratio is kept constant at 7.5. Furthermore, the ratio of radial to circumferential dimensions of the PPs, the airgap lengths, and the inner airgap diameter are kept constant. It can be seen, that a minimum copper mass

or total active mass can be achieved, however, the PM mass may not be minimum. If only designs with a minimum PM mass are considered, a minimum active mass can be achieved for a number of sections of about 20. It can also be seen, that when the number of sections is decreased the total active mass considerably increases, which is mainly due to the increased back iron mass.

Fig. 15 and Fig. 16 show the variations of the copper and total active mass with the PM mass and the gear ratio, where the equivalent shearstress at pullout torque is 100kPa and the designs have the same number of segments as the PDDs in Table I. It can be seen, that the minimum PM mass does not vary significantly for the range of gear ratios from 5.5 to 8.5, and that also the total active mass and copper mass do not vary significantly over this range for these designs.

Fig. 17 shows the variations of the active masses in 6m and 8m airgap diameter PDDs with the PM mass, where the equivalent shear stress at pullout torque is 100kPa, and the gear ratio is 7.5. It can be seen, that for a given PM mass a PDD may be realised at an airgap diameter of less than 8m, however this can only be achieved at the expense of increased copper and laminated steel mass.

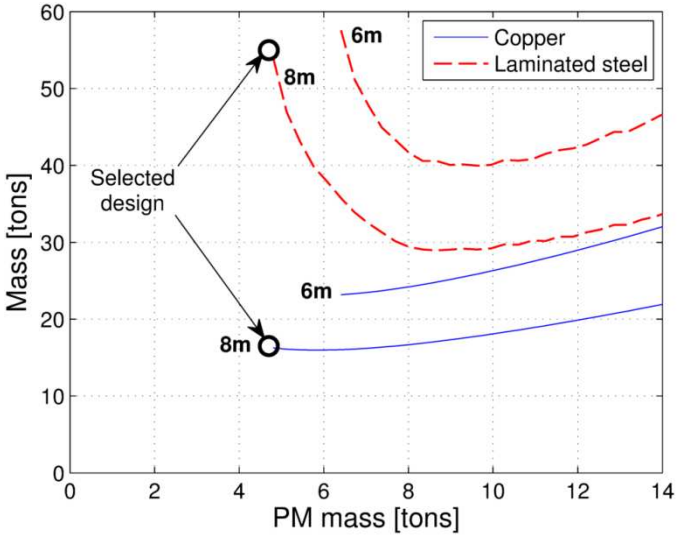

Fig. 17. Variation of active masses with the PM mass, when the shearstress is 100kPa, the gear ratio is 7.5 and the copper loss is fixed to 4.0%.

Since the analytical method assumes infinitely permeable steel and doesn't take into account of saturation, FE has subsequently been used in order to further optimize the selected design given in Table I and shown in Fig. 17. The PM mass of the selected design is 4.5tons, which is less than for a similar PM direct drive, where a PM mass of 6tons has been reported [14], and significantly smaller than for a similar PDD with HS rotor PM excitation, where the PM mass is 13.5tons [9]. Due to the volatility of the PM magnet price [15] employing a coil excited PDD may provide increased stability to the cost of the drive train. For example, Table II gives the manufactured cost for the active materials of a PM excited and a coil excited PDD for a scenario, where the cost of the PM material is close to the current market value (Scenario 1), and a scenario where the cost is increased and of similar magnitude as the price in 2011 (Scenario 2). The copper and steel prices are assumed to be unchanged. It can be seen, that for the PM excited PDD the manufactured cost for the total active material could increase by more than 140%, while for a coil excited PDD the cost is only 70% higher in Scenario 2. However, compared to the PDD with HS rotor PM excitation the coil excited PDD has a lower efficiency and increased copper and active steel mass. Furthermore, a coil excited 10MW PDD could be achieved with an airgap diameter of less than 8m.

TABLE II
COST COMPARISON OF 10MW PDDS

Quantity	PM excited PDD [9]	Coil excited PDD, Table I
Electromagnetic efficiency at rated power [%]	99	95
PM mass [tons]	13.5	4.5
Copper mass [tons]	7	20
Active steel mass [tons]	36	59
Scenario 1		
Manufactured cost for PM material	60k€/ton	
Manufactured cost for copper	15k€/ton	
Manufactured cost for laminated steel	3k€/ton	
Total active material cost	1128 k€	747 k€
Scenario 2 – high PM price		
Manufactured cost for PM material	180k€/ton	
Manufactured cost for copper	15k€/ton	
Manufactured cost for laminated steel	3k€/ton	
Total active material cost	2748 k€	1287 k€

V. CONTROL OF THE PDD

The generator may be connected to the grid employing a power electronic converter equipped with an active rectifier dc link and a grid inverter, as it would be the case for a conventional PM generator. However, since the excitation of the rotor can be actively controlled the active rectifier may be replaced by a passive diode rectifier, resulting in less costly, simpler and more reliable power electronics. In any case the generator should be controlled to maximize efficiency. Similarly to conventional wound field machines the HS rotor winding could be supplied through slip rings and brushes, or using a brushless exciter system [16].

The electromagnetic losses in the coil excited PDD can be separated into the copper losses in the HS rotor windings P_H, the copper losses in the stator windings P_S and the iron losses in the laminations P_{iron}. These losses are dependent on I_f, I_S and the rotational speed Ω of the PDD, and can be expressed as:

$$P_{loss} = P_H(I_f) + P_S(I_S) + P_{iron}(I_f, I_S, \Omega) \tag{45}$$

where

$$P_H(I_f) = R_H I_f^2 \tag{46}$$

$$P_S(I_S) = 3R_S I_S^2 \tag{47}$$

where R_H and R_S are the resistances of the HS rotor and stator coils respectively, calculated at the operating temperature of

120°C. Furthermore, in order to simplify the analysis and minimize the losses without the need for extensive and time consuming finite element analysis, the iron losses have been assumed to be given by the following analytical expression of I_f, I_S and Ω:

$$P_{iron}(I_f, I_S, \Omega) = \Omega\,(c_{h,f} I_f^2 + c_{h,S} I_S^2) \quad \text{(hysteresis)} \quad (48)$$
$$+\Omega^2 (c_{c,f} I_f^2 + c_{c,S} I_S^2) \quad \text{(classical eddy currents)}$$
$$+\Omega^{1.5} \left(c_{e,f} I_f^2 + c_{e,S} I_S^2\right)^{0.75} \quad \text{(excess eddy currents)}$$

$c_{h,f}$, $c_{h,S}$, $c_{c,f}$, $c_{c,S}$, $c_{e,f}$ and $c_{e,S}$, are coefficients, determined from a selected number of iron loss predictions using finite element analysis. Therefore, the coefficients $c_{h,f}$, $c_{c,f}$ and $c_{e,f}$ are determined by a single iron loss prediction on no-load condition, i.e. $I_S = 0$, while $c_{h,S}$, $c_{c,S}$ and $c_{e,S}$, are subsequently determined when the machine is fully loaded. Furthermore, the stator PMs experience time variations in their operating points, which will induce eddy currents. However, their magnitudes depend on the level of segmentation, and the associated losses are typically small for this type of machine and are, therefore, neglected in this analysis.

From equations (45)-(48) the coil excited PDD can be controlled so as to minimize the electromagnetic losses, while satisfying the operational requirements/constraints as follows:

$$T_{pull} \geq 1.2 \times \text{turbine torque} \quad (49)$$
$$EMF \geq \text{minimum } EMF \quad (50)$$
$$I_S \leq \text{rated stator current} \quad (51)$$
$$I_f \leq \text{rated HS rotor current} \quad (52)$$

As long as the rated currents are not exceeded the minimum EMF would be limited by the required boosting and the resulting ripple in the current and its effects on the efficiency of the machine and the size of the required filter.

In the analysis the variations of the power coefficient and the rotor speed have been selected similar to those adopted in INNWIND.EU reference turbine [11], where the rotational speed of the turbine varies between 6.0 and 9.6rpm. As an example Fig. 18 shows the variation of the EMF of the PDDs with coil excited and PM excited HS rotors with the wind speed, where the minimum EMF for the coil excited PDD is kept the same as for the PM excited PDD, in order to allow for a more appropriate comparison with the PM excited PDD. It can be seen, that in order to minimize the electromagnetic losses the EMF may have to be reduced faster than the rotational speed.

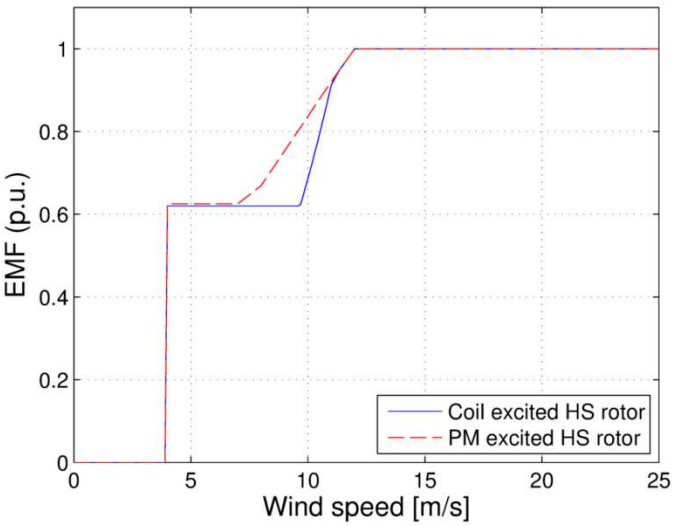

Fig. 18. Variation of the EMF with the wind speed for a PDD with HS rotor coil excitation and for a PDD with PM excited HS rotor. (EMF per unit of the rated EMF)

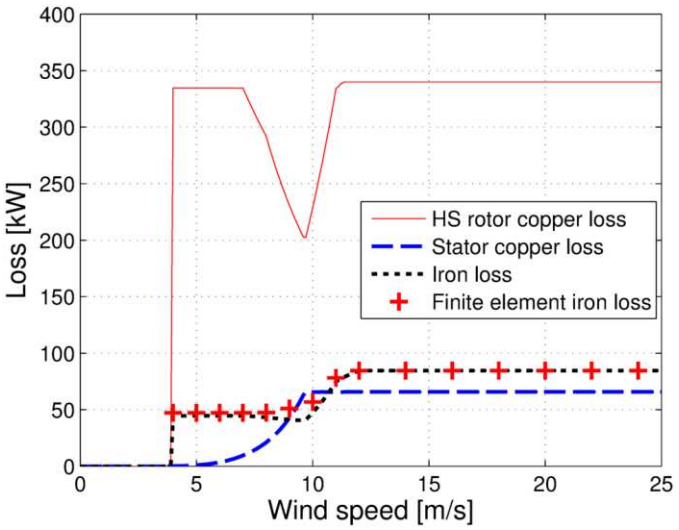

Fig. 19. Variation of the losses with the wind speed.

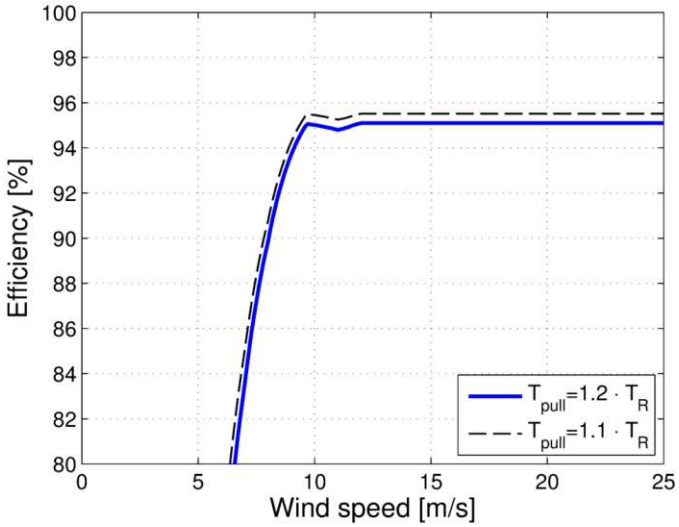

Fig. 20. Variation of the efficiency with the power. (Pullout torque per unit of rated torque T_R)

Fig. 19 shows the variation of the resulting copper and iron losses with the wind speed. It can be seen, that the HS rotor copper losses are relatively large compared to the other losses. Therefore, in this case in order to minimise the losses the stator current remains constant until the minimum EMF is reached. In general in a PDD the stator losses are inherently lower compared to direct drives and other PM machines. Therefore, although the HS rotor losses are relatively high to

the stator losses in this machine, they are not very high in absolute terms. Nevertheless due to their location on the rotor special forced air cooling should be considered.

Fig. 20 shows the variation of the efficiency with the wind speed. It can be seen, that the efficiency remains fairly constant until the excitation current is increased to ensure the EMF remains above the minimum value. It can also be seen, that efficiency improvements can be realized, if the constraint in (49) is relaxed and the PDD is allowed to operate closer to the pullout torque. This is possible because of the extra degree of controllability enabled by the coil excitation.

In order to assess the annual energy efficiency a Weibull probability distribution for the wind speed frequency is adopted [12]:

$$p(v) = \frac{k}{A}\left(\frac{v}{A}\right)^{k-1} \exp\left[-\left(\frac{v}{A}\right)^{k}\right] \qquad (53)$$

where v is the wind speed, $k = 2.35$ is the shape parameter and A=12.01m/s is the scale parameter, which have been selected to fit a measured wind profile at a height of 110m at the FINO3 offshore research platform in the north sea [13], as can be seen in Fig. 21.

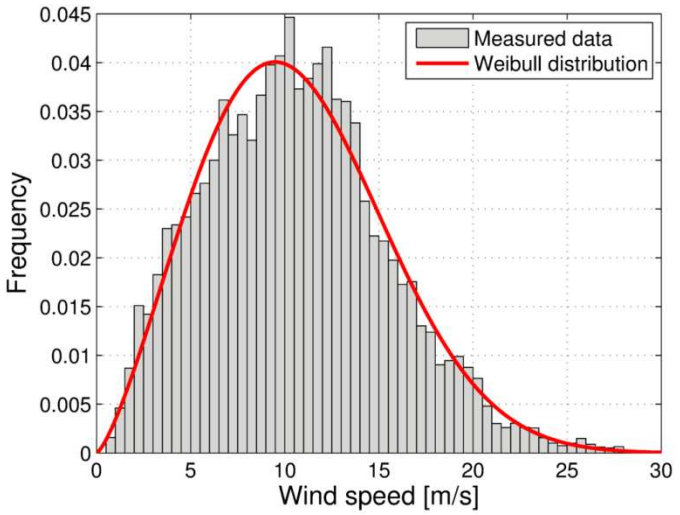

Fig. 21. Frequency of the wind speeds at the research platform FINO3 at 110m height for the year 2011 [13]. The Weibull distribution has been fitted to the measured data.

Fig. 22 shows the variation of the annual energy efficiency with the minimum EMF for the PDDs with coil excitation and PM excitation. Designs for which constraints (50) and (52) could not be fulfilled simultaneously over the entire range of the operating wind speeds have been rejected in this analysis. In particular for this PDD, the minimum EMF had to be kept below 62% of the rated EMF. It can be seen, that the selection of the minimum EMF has a significant effect on the annual energy efficiency and this should be considered, when a control strategy and a converter topology are selected. It can also be seen that the efficiency of a PM excited PDD could exhibit a significantly higher annual energy efficiency, however, the PM excited PDD would also require a significantly larger amount of PMs.

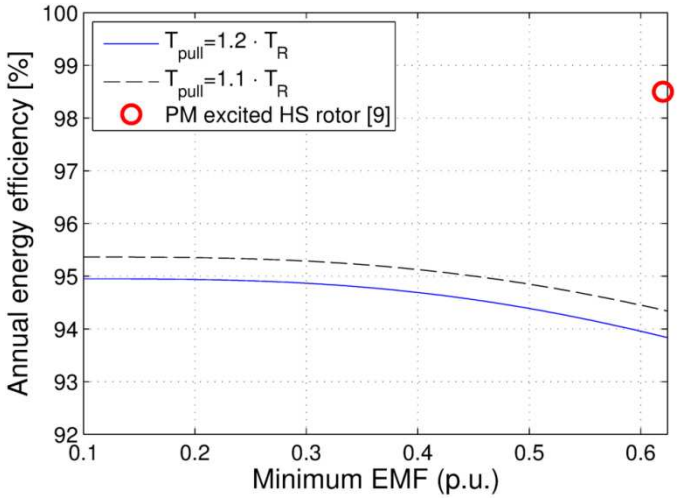

Fig. 22. Variation of the annual energy efficiency with the minimum EMF. (Minimum EMF per unit of the rated EMF, and pullout torque per unit of rated torque T_R)

VI. Conclusion

A model for the analytical prediction of the flux density distribution in the airspaces and PMs of coil excited HS rotor PDDs is presented. It has been shown, that a good agreement exists between the analytical and FE predictions. Furthermore, the analytical models have been employed for the optimisation of a 10MW coil excited PDD for a wind turbine. It has been shown that shear stress in excess of 100kPa can be achieved, and that significant reductions in PM mass can be realized compared to a PDD with HS rotor PM excitation, albeit at the expense of increased total active mass and reduced efficiency. However, it has also been shown, that controlling the excitation current is necessary, in order to maximise the annual energy efficiency.

References

[1] P. M. Tlali, R. J. Wang, and S. Gerber, "Magnetic gear technologies: A review," in Electrical Machines (ICEM), 2014 International Conference on, Sept 2014, pp. 544–550.

[2] K. Atallah and D. Howe, "A novel high-performance magnetic gear", IEEE Trans. Magn., vol. 37, no. 4, pp. 2844 --2846, Jul. 2001.

[3] P. Rasmussen, T. Andersen, F. Jorgensen, and O. Nielsen, "Development of a high-performance magnetic gear," Industry Applications, IEEE Transactions on, vol. 41, no. 3, pp. 764–770, 2005.

[4] L. Jian, K. Chau, and J. Jiang, "A magnetic-geared outer-rotor permanent-magnet brushless machine for wind power generation," Industry Applications, IEEE Transactions on, vol. 45, no. 3, pp. 954–962, 2009.

[5] Atallah, K. and Rens, J. and Mezani, S. and Howe, D., "A Novel 'Pseudo' Direct-Drive Brushless Permanent Magnet Machine", Magnetics, IEEE Transactions on Magnetics 44, 11 (2008), pp. 4349 -4352.

[6] H. Polinder, J. Ferreira, B. Jensen, A. Abrahamsen, K. Atallah, and R. McMahon, "Trends in wind turbine generator systems," Emerging and Selected Topics in Power Electronics, IEEE Journal of, vol. 1, no. 3, pp. 174–185, Sept 2013.

[7] A. Penzkofer and K. Atallah, "Magnetic gears for high torque applications," Magnetics, IEEE Transactions on, vol. 50, no. 11, pp. 1–4, Nov 2014.

[8] T. Lubin, S. Mezani, and A. Rezzoug, "Analytical computation of the magnetic field distribution in a magnetic gear," Magnetics, IEEE Transactions on, vol. 46, no. 7, pp. 2611 –2621, July 2010.

[9] A. Penzkofer and K. Atallah, “Analytical modelling and optimisation of pseudo direct drive permanent magnet machines for large wind turbines,” Magnetics, IEEE Transactions on, 2015.
[10] Zhu, Z.Q. and Howe, D., "Instantaneous magnetic field distribution in brushless permanent magnet DC motors. II. Armature-reaction field", Magnetics, IEEE Transactions on 29, 1 (1993), pp. 136-142.
[11] C. Bak, et.al., “Description of the DTU 10MW reference wind turbine”, Report Number: DTU Wind Energy Report-I-0092, Jun 2013.
[12] Eugene C. Morgan, Matthew Lackner, Richard M. Vogel, Laurie G. Baise, ”Probability distributions for offshore wind speeds”, Energy Conversion and Management, vol. 52, Issue 1, pp. 15-26, Jan 2011.
[13] I. Bastigkeit, et.al. “Database of existing wind parameter measurements for tall atmospheres across Europe”, INNWIND.EU, Work package 1: Conceptual designs, Task 1.1: External conditions, Report deliverable D1.11, Aug 2014.
[14] H. Polinder, D. Bang, R. P. J. O. M. Van Rooij, A. McDonald, and M. Mueller, “10 MW wind turbine direct-drive generator design with pitch or active speed stall control,” in Electric Machines Drives Conference, 2007. IEMDC ’07. IEEE International, vol. 2, 2007, pp. 1390–1395.
[15] J. J. Pyrhönen, Y. Alexandrova, R. S. Semken and H. Hämäläinen, "Wind power electrical drives for permanent magnet generators; Development in Finland", ELEKTRO, 2012, Rajeck Teplice, pp. 9-16, 2012.
[16] T. L. Dillman, F. W. Keay, C. Raczkowski, J. W. Skooglund and W. H. South, "Brushless excitation," in IEEE Spectrum, vol. 9, no. 3, pp. 58-66, March 1972.